



# Interferometric near-field characterization of plasmonic slot waveguides in single- and poly-crystalline gold films

M. PRÄMASSING,<sup>1</sup> M. LIEBTRAU,<sup>1</sup> H. J. SCHILL,<sup>1</sup> S. IRSEN,<sup>2</sup> AND S. LINDEN<sup>1,\*</sup> 

<sup>1</sup>Physikalisches Institut, University of Bonn, D-53115 Bonn, Germany

<sup>2</sup>Center of advanced european studies and research (caesar), D-53175 Bonn, Germany

\*linden@physik.uni-bonn.de

**Abstract:** Single-crystalline gold films show superior plasmonic properties compared to their poly-crystalline counterparts. However, this advantage comes at the cost of a more complex preparation process. It is thus crucial to validate whether the impact of the material quality on the performance of the respective plasmonic device justifies this additional effort. In order to address this question for the case of plasmonic slot waveguides, we present interferometric near-field measurements at telecommunication wavelengths on slot waveguides in single- and poly-crystalline gold films. We observe significantly larger propagation lengths in the case of single-crystalline gold films for slot widths below 100 nm. In contrast for larger widths, both gold films give rise to comparable propagation lengths.

© 2020 Optical Society of America under the terms of the [OSA Open Access Publishing Agreement](#)

## 1. Introduction

Plasmonic waveguides can support guided surface plasmon polaritons (SPPs) with deep-subwavelength mode cross-sections [1]. This feature distinguishes plasmonic waveguides for applications in which the tight lateral confinement of the electromagnetic energy is paramount. For instance, the possibility to undercut the diffraction limit imposed on dielectric waveguides makes their plasmonic counterparts attractive for integrated nanophotonic circuits. In this context, a number of components based on plasmonic waveguides have been recently demonstrated, e.g., nanolasers [2], modulators [3], directional couplers [4,5] and nanodetectors [5]. Plasmonic waveguides are also a promising platform for nanoscale quantum optics. Here, one exploits the enhancement of the local electromagnetic density of states provided by plasmonic waveguides [6–8].

In recent years, a wide range of different plasmonic waveguide geometries have been proposed and studied experimentally, e.g., metal nano-wires [8–11], metal stripes [12,13], arrays of metallic nano-particles [14,15], wedges [16], and v-shaped grooves in metal films [17,18]. One of the most promising configurations with respect to the implementation of planar, on-chip-compatible integrated nanophotonic circuits and opto-electrical interconnects is the plasmonic slot waveguide (PSW) [19,20] or the closely related two-wire transmission line [21]. The PSW comprises a narrow, rectangular slot in a thin metal film [3,4,22] and its fundamental SPP mode is strongly confined to the slot region (see Fig. 1(a) for a schematic representation of a PSW and (b) for the calculated SPP mode profile). As a very promising application, a quantum emitter can be deposited in the slot region. Due to the huge optical density of states resulting from the extreme mode confinement, the quantum emitter can couple to the guided SPP mode very efficiently [23,24].

Scanning near-field optical microscopy (SNOM) has become an indispensable tool to study the near-field of plasmonic nanostructures [25–29]. In particular, scattering-type SNOM (s-SNOM) in combination with pseudoheterodyne detection is a versatile technique for the characterization

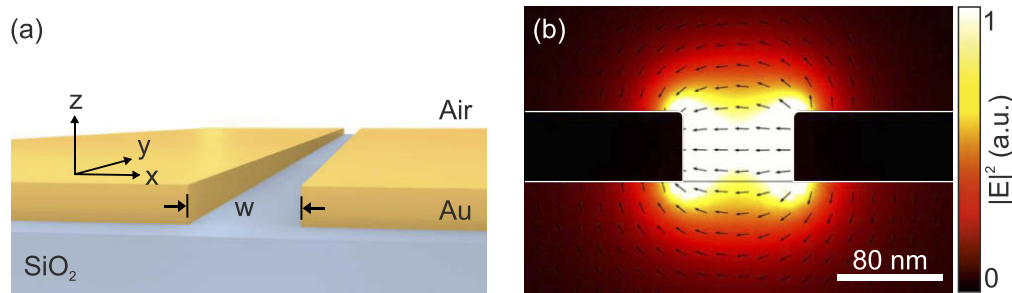


**Fig. 1.** (a) Schematic representation of a plasmonic slot waveguide. (b) Calculated intensity distribution of the guided plasmonic mode. The black arrows indicate the orientation of the transverse electric field component.

of plasmonic waveguides [9,13,30–33] as it allows to measure the amplitude and phase of the waveguide mode from which one can infer its effective index  $n$  as well as its propagation length  $L$ . For instance, this technique has been applied to investigate the modes supported by plasmonic strip waveguides [13] and to study the coupling of free space radiation to the PSW mode by different dipole antenna couplers [31].

A handicap of many plasmonic waveguides that goes hand in hand with the tight transversal field confinement is the limited mode propagation length. Typical experimental values range between several microns and tens of microns at optical frequencies. A significant contribution to the damping of the guided SPP modes can be attributed to Ohmic losses inside the metal. Other possible loss channels are connected with optical scattering from fabrication imperfections and leakage radiation into the substrate. A possible solution to overcome the limitations resulting from the rather short propagation lengths is to interface plasmonic waveguides with low-loss dielectric waveguides [7,33]. Another approach to optimize the performance of plasmonic waveguides and plasmonic nanostructures in general is to improve the structural and intrinsic material quality of the utilized metallic film. It has been proposed and tested by Huang et al. in 2010 that the use of chemically synthesized single-crystalline gold flakes in combination with focused ion beam milling results in plasmonic nanostructures of superior quality compared to structures fabricated on thermally evaporated gold films [34]. This eliminates grain boundary scattering as an important plasmon loss mechanism [35]. It has been shown in several experiments that the use of single-crystalline metallic nanostructures can improve their linear and nonlinear optical properties [21,23,36,37].

The preparation of suitable single-crystalline gold films involves considerably higher experimental effort compared to the evaporation of poly-crystalline gold films. For instance, the chemical synthesis of the single-crystalline flakes is time consuming and critically dependent on the experimental conditions and quality of the applied chemicals. Additionally the yield of flakes, which are actually usable for further processing through focused ion beam milling i.e. flakes that have the desired thickness and sufficient lateral size, is rather low. The selection of the flakes in order to match these requirements is another time consuming step, since it involves characterization by optical microscopy and atomic force microscopy. This may raise the question if the fabrication of single-crystalline plasmonic structures is always profitable, i.e. if the impact of the material quality on the performance of plasmonic devices justifies the additional effort. Surprisingly, quantitative comparisons of SPP propagation length between single-crystalline and poly-crystalline films are rarely present in the literature [35,38,39]. To the best of our knowledge, the only quantitative comparison for guided plasmon polaritons is available for silver nanowires [40,41]. Our work addresses this issue and provides the first direct comparison of PSWs in single-crystalline and poly-crystalline gold films via interferometric near-field characterization.

We investigate PSWs with variable gap sizes down to 50 nm utilizing s-SNOM in transmission mode configuration. This approach allows us identifying two regimes with different dominant loss channels. In the first regime of very small gap sizes, the Ohmic losses are dominant and the material quality has a significant impact on the mode propagation length. In contrast, for large gap sizes, where the waveguide mode exhibits a lower field confinement, the material quality has almost no influence on the mode propagation length. Our experimental findings are in quantitative agreement with numerical three-dimensional (3D) finite element calculations.

## 2. Samples and experiment

The single-crystalline gold films are fabricated by chemical synthesis in solution [42]. A mixture of 40  $\mu\text{l}$  of a 0.5 molar aqueous solution of chloroauric acid  $\text{HAuCl}_4$  and 20 ml ethylene glycol is filled into a polypropylene tube. A glass coverslip is immersed into the solution and the tube is heated up to 90  $^\circ\text{C}$  in an oven for 20 h. Gold atoms released in a three-step chemical reaction can form single-crystalline gold flakes of varying heights and lateral sizes on the glass coverslip. Typically, flakes with large lateral dimensions of several tens up to 100  $\mu\text{m}$  exhibit a thickness of a few tens of nanometers, whereas flakes with lateral sizes smaller than 10  $\mu\text{m}$  are often thicker than 100 nm (see Fig. 2(a)). The glass coverslip is removed from the ethylene glycol solution and immersed in acetone. The remaining ethylene glycol dissolves in the acetone and the flakes detach from the glass coverslip.

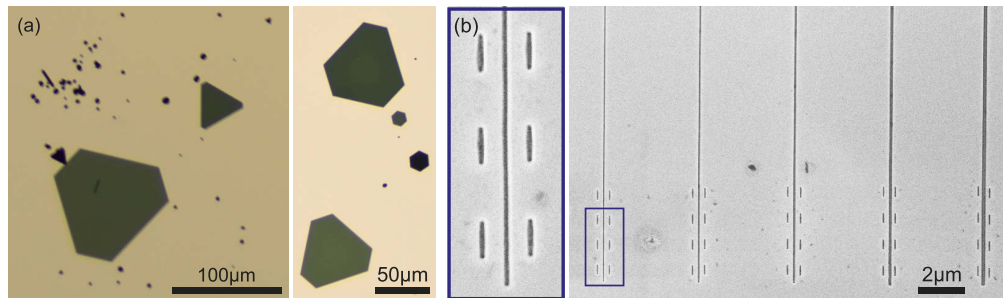


**Fig. 2.** (a) Optical transmission microscope images of chemically synthesized single-crystalline gold flakes. (b) Scanning electron microscopy images of the investigated PSWs in the single-crystalline film. The blue box displays an enlarged view of the phasematched slot-dipole-antenna array at the 50 nm PSW.

Subsequently, the flakes are transferred by dropcasting from the acetone solution onto a glass substrate, which is coated with a thin layer of Indium Tin Oxide (ITO). Upon evaporation of the acetone, the flakes tightly attach to the ITO via surface adhesion forces. The adhesion proves strong enough to permit AFM measurements at the edge. In an additional experiment we have shown that the flakes even remain in contact with the substrate when atomically thin Van der Waals materials are transferred onto the flake by a PDMS (polydimethylsiloxan) stamp. The electrical conductivity of the ITO layer ensures compatibility of the samples with scanning electron/ion microscopy, while preserving optical transparency for near-infrared wavelengths. We use optical microscopy in combination with atomic force microscopy (AFM) to select a sufficiently large flake with a thickness of 50 nm for further processing. For comparison, we also prepare a poly-crystalline gold film by thermal evaporation of a 2 nm-thin chromium adhesion layer and a 50 nm thick gold film onto a glass substrate. In the next step, the PSWs are patterned into the gold films by focused ion beam milling (Zeiss XB1540 crossbeam). We utilize  $\text{Ga}^{2+}$  ions with an acceleration voltage of 30 kV and a beam current of 1.5 pA. Figure 2(b) shows scanning electron micrographs of a set of five waveguides milled into the single-crystalline gold

film. The slot width  $w$  increases from  $w = 50$  nm to  $w = 150$  nm from left to right. An enlarged view of the end of the  $w = 50$  nm PSW is shown in the blue box. A phase-matched array of four pairs of slot-dipole antennas is milled into the surrounding metal film at the end of each PSW, providing an efficient interface to couple free-space radiation to the waveguide mode. The single slot-antennas are designed to be resonant at telecommunication wavelengths with a length of 420 nm and a width of 60 nm. The center-to-center distance of a slot antenna to the waveguide is 250 nm. The period of the antenna array varies from 980 nm to 1080 nm in order to match the effective wavelength of the waveguide mode for the different slot width.

The near-field of the PSWs is characterized with a s-SNOM (Neaspec neaSNOM) in transmission mode configuration. The setup is schematically depicted in Fig. 3(a). The attenuated beam of a tunable near-infrared femtosecond light source (Stuttgart Instruments Alpha-HP) tuned to a wavelength of 1520 nm is spatially filtered by a single mode fiber and focused onto the antenna coupler array from below by a parabolic mirror. The waist radius of the Gaussian beam at the sample surface is determined to be approximately  $4\ \mu\text{m}$  by a knife edge measurement. The incident beam is polarized along the  $x$ -direction to resonantly excite the slot-antenna array and efficiently couple to the waveguide mode, which propagates along the slot in  $y$ -direction. A metallized AFM tip (Nanoworld Arrow NCPT) is approached to the sample by means of tapping mode atomic force microscopy. Due to its elongated shape in vertical direction, the tip acts as an antenna, predominantly scattering the out-of-plane near-field component  $E_z$  at the sample surface to the far-field. The scattered radiation is collimated and guided to an Indium-Gallium-Arsenide detector by the upper parabolic mirror. To measure both the amplitude and phase of the near-field by psudoheterodyne detection [43], the scattered signal is overlapped with a reference beam. Demodulation of the detector signal at higher harmonics of the tip oscillation frequency  $\Omega$  allows to strongly suppress background contributions, e.g. light directly scattered from the sample or the tip. By raster scanning the sample with respect to the fixed configuration of the tip and the

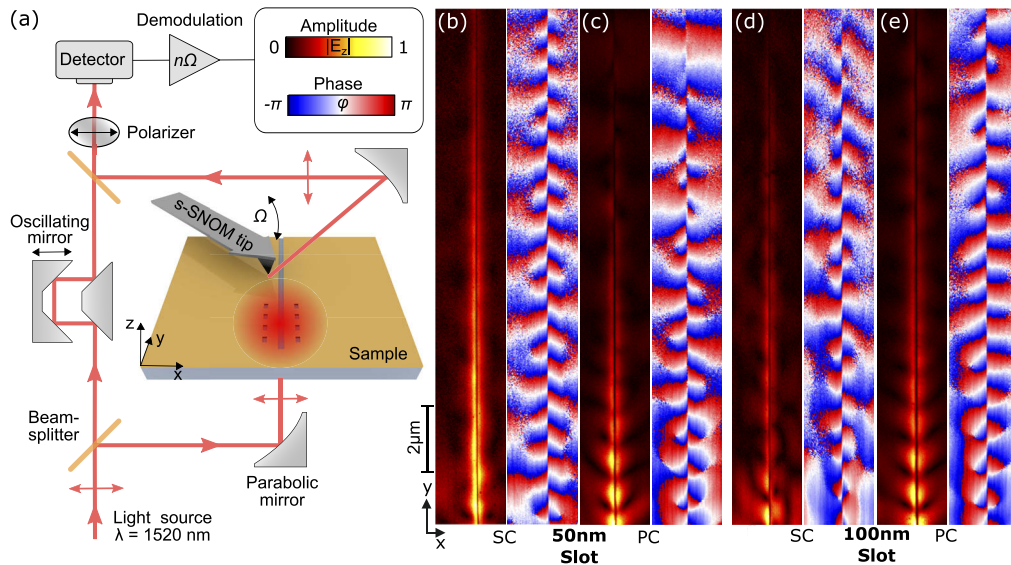


**Fig. 3.** (a) Scheme of the scattering type scanning near-field optical microscope in transmission mode configuration. Amplitude  $|E_z|$  and phase  $\varphi$  data of the measured near-field distribution of PSWs with different gap widths  $w$  in single-crystalline (SC) and thermally evaporated poly-crystalline (PC) gold films: (b)  $w = 50$  nm, SC; (c)  $w = 50$  nm, PC; (d)  $w = 100$  nm, SC; (e)  $w = 100$  nm, PC. The signals are in each case demodulated at the third harmonic of the tip oscillation frequency ( $n = 3$ ).

upper parabolic mirror we obtain a two-dimensional (2D) map of the near-field distribution. A synchronized movement of the lower parabolic mirror along with the sample guarantees a fixed illumination of the antenna coupler array during the scan. Movements of the lower parabolic mirror along  $x$ -direction require a correction of the phase raw-data by an additive contribution  $\varphi_{\text{raw}}$  to account for the change of the optical path length with respect to the reference arm of the interferometer:  $\varphi = \varphi_{\text{raw}} + 2\pi \frac{x}{\lambda}$ . Movements along the  $y$ -direction require no phase correction, since they do not alter the optical path length.

### 3. Results and discussions

Figure 3(b) shows amplitude and phase data of a near-field measurement along a  $w = 50$  nm wide PSW in single-crystalline gold, demodulated at the third harmonic of the tip oscillation frequency. The tapping amplitude of the tip is set to 70 nm and the wavelength of the incident laser is 1520 nm for all measurements. The antenna array, which excites the waveguide mode is not included in the scan region and lies further below in negative  $y$ -direction. The near-field amplitude  $|E_z|$  is tightly confined around the slot in  $x$ -direction and decreases during mode propagation along the  $y$ -direction. As expected from the transverse electric field distribution depicted in Fig. 1(b), the measured out-of-plane field component  $|E_z|$  vanishes in the middle of the slot. The corresponding phase data clearly displays the expected antisymmetric nature of the mode with a phase jump of  $\pi$  across the slot. During mode propagating, we observe a linear phase increase in  $y$ -direction.

The experimental data for the  $w = 50$  nm wide PSW milled into the poly-crystalline gold film is shown in Fig. 3(c). It is immediately apparent that the propagation length is here significantly shorter than in the previous case. For that reason, we had to move the scan region closer to the excitation such that the exciting beam partially overlaps with the scan region. Therefore, we have a significant contribution of free propagating SPPs on the gold/air interface excited by the incident beam on the edges of the slot. The interference of the waveguide mode propagating in  $y$ -direction and the SPPs running in  $\pm x$ -direction results in the observed beating pattern [31].

Figure 3(d) and (e) display the amplitude and phase maps of PSWs with a slot width of  $w = 100$  nm milled into the single-crystalline gold film and the poly-crystalline gold film, respectively. In contrast to the case of the  $w = 50$  nm wide slot, we now observe comparable propagation lengths for both film types. Again, the beating pattern can be attributed to the interference of the slot mode with freely propagating SPPs.

In order to extract the effective mode index  $n$  and the propagation length  $L$  of the waveguide mode from the measured near-field distributions, we fit the following 2D model, which describes the  $E_z$ -component of the waveguide mode outside of the gap region, to the data:

$$E_z(x, y) = \begin{cases} E_r \exp[y(ik_0 n - \frac{1}{2L}) - \frac{x-x_0}{\kappa} + \varphi_0] & x - x_0 \geq w/2 \\ -E_l \exp[y(ik_0 n - \frac{1}{2L}) - \frac{x_0-x}{\kappa} + \varphi_0] & x_0 - x \geq w/2 \end{cases}. \quad (1)$$

In this model, the center of the slot is located at  $x = x_0$ . The gap region is excluded from the fit. We allow different values for the amplitudes  $E_r$  and  $-E_l$  on the right and left hand-side of the gap to account for the slight asymmetry of the near-field amplitude in the measurements, which we attribute to the specific geometry of the detection optics in the s-SNOM. i.e., the relative positions of the slot with respect to the AFM tip and the collecting parabolic mirror. The opposite algebraic signs take the phase jump of  $\pi$  across the slot into account,  $\varphi_0$  represents a global phase and  $k_0 = 2\pi/\lambda_0$  is the free space wavenumber. The evanescent decay of the mode away from the slot region is described by the parameter  $\kappa$ .

Figure 4(a) exemplarily shows the  $E_z$  component of the experimental data and of the fitted 2D model for the case of the  $w = 50$  nm wide PSW milled in the single-crystalline film. The resulting parameters for the propagation length  $L$  and the effective mode index  $n$  for gap widths

are plotted in Fig. 4(b) and (c), respectively. The error bars result from averaging fit results from the measurement data of the third and fourth demodulation order as well as the forward and backward scan direction, respectively. For the single- as well as the poly-crystalline gold film, the effective mode index decreases with increasing gap size. This behaviour is expected from theoretical considerations [20] (also see below). In the poly-crystalline film, the mode index is slightly larger than that of the single-crystalline sample. We attribute this to the influence of the 15 nm thin ITO layer that we had to deposit on the glass substrate in the case of the single-crystalline gold film for fabrication reasons and that is absent in the case of the evaporated gold film. For the thinnest waveguide in the poly-crystalline film, the effective mode index deviates from the expected monotonic increase when lowering the slot width. We attribute this behavior to fabrication imperfections during focused ion beam milling. Since the field enhancement in the slot region is higher for thinner slots, we expect imperfections like grains on the edges to have larger influence in this case. Since the 50 nm slot width represents the fabrication limit for our FIB microscope in combination with the poly-crystalline films, it is also possible that some residual metal remains in the slot region, which could affect the effective mode index. In contrast, for single-crystalline films even finer slots of 40 nm can be fabricated.

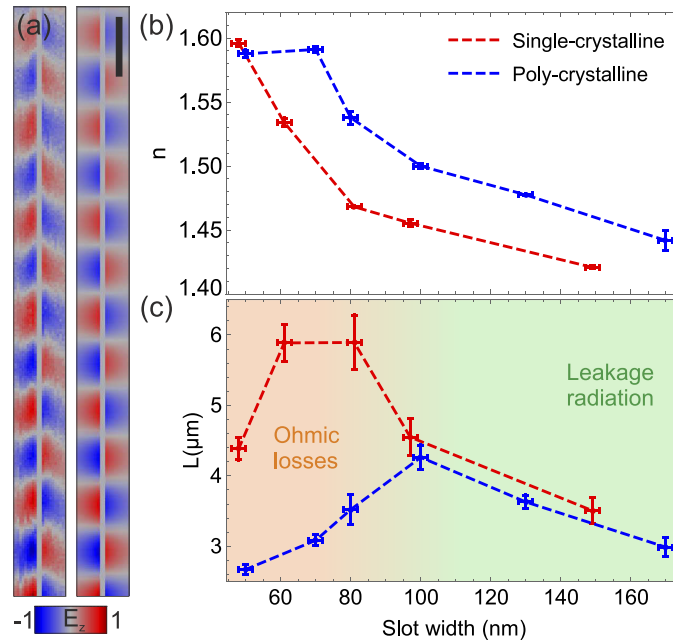


**Fig. 4.** Results of the 2D complex fits. (a) Real part of the  $E_z$  electric field component around the  $w = 50$  nm slot in the single-crystalline film: Measured data (left panel) and fit (right panel). The scale bar has a length of 500 nm. Effective mode indices (b) and propagation lengths (c) both on poly-crystalline and single-crystalline gold for different slot width.

Interestingly, the propagation length shows for both films a non-monotonic behaviour. In the case of the single-crystalline gold film, we observe a maximum propagation length of  $L \approx 6 \mu\text{m}$  for a gap width of  $w = 80$  nm. The maximum propagation length for the poly-crystalline gold film is about  $L \approx 4 \mu\text{m}$  reached for a gap width of  $w = 100$  nm. We explain this non-monotonic behaviour by a trade-off between two different loss channels. With decreasing gap size, a larger fraction of the electric field resides in the metal and the Ohmic losses increase. In this region, we expect that the quality of the gold film plays a crucial role. This is in accordance with our

observation that for gap sizes below  $w = 100$  nm the propagation length of the PSWs defined in the single-crystalline gold film is up to a factor two larger than that of the PSWs in the poly-crystalline gold film. In contrast, for large gap sizes, we expect that the Ohmic losses are reduced since a larger fraction of the electric field of the mode is located in the gap region and in the dielectric surrounding of the metal film. Hence, one could naively expect that  $L$  should monotonically increase with the gap size. Nevertheless, we observe a different behaviour, i.e., the propagation length decreases for the largest gap sizes for both gold films. The reason for this is leakage radiation, which becomes the dominant loss channel once the effective mode index deceeds the refractive index of the substrate. As a result, we observe for both gold films comparable propagation lengths in the case of large gap sizes above  $w = 100$  nm.

In order to support this interpretation, we have performed 3D numerical calculations employing a commercial finite element method solver (COMSOL Multiphysics). The total size of the computational domain is  $1.5 \mu\text{m} \times 20 \mu\text{m} \times 3 \mu\text{m}$  ( $x \times y \times z$ ). We take advantage of the symmetry of the PSW by applying perfect electric conductor boundary conditions to the  $yz$ -plane in the middle of the gap. All other boundaries of the computational domain are terminated by perfectly matched layers with a thickness of 750 nm. The 50 nm gold film is sandwiched between the glass substrate below (refractive index  $n=1.5$ ) and air (refractive index  $n=1$ ) above. The gap region consists of air. For the dielectric function of the gold film, we use the data provided by Johnson and Christy [44]. The slot waveguide has a length of  $18.5 \mu\text{m}$  and is terminated in  $y$ -direction on one end by  $1.5 \mu\text{m}$  of gold and on the other end by a perfectly matched layer. For reasons of calculation time and memory consumption, we omit the phase-matched slot-dipole-antenna array and excite the slot mode at the closed end of the waveguide by a normally incident,  $x$ -polarized Gaussian beam from the substrate side. The slot width is varied in a parameter sweep from  $w = 40$  nm to  $w = 150$  nm in steps of 10 nm. From each of these calculations, we extract the transverse electric field component  $E_x(y)$  along a line profile through the center of the slot in propagation direction ( $y$ -direction). The effective mode index and the propagation distance are obtained by fitting a one-dimensional damped harmonic wave to the  $E_x(y)$ -data (see Fig. 5). The numerical results are in good agreement with the experimental findings for the single-crystalline gold film. In particular, they also show a monotonic decrease of the effective mode index and a maximum of the propagation length for gap sizes around  $w \approx 90$  nm. As in the experiment, we observe that the propagation length strongly decreases once the effective mode index becomes smaller than the refractive index of the substrate. We note that the latter aspect cannot be reproduced with 2D mode analysis calculations, in which leakage of the slot mode into the substrate is not properly taken into account.

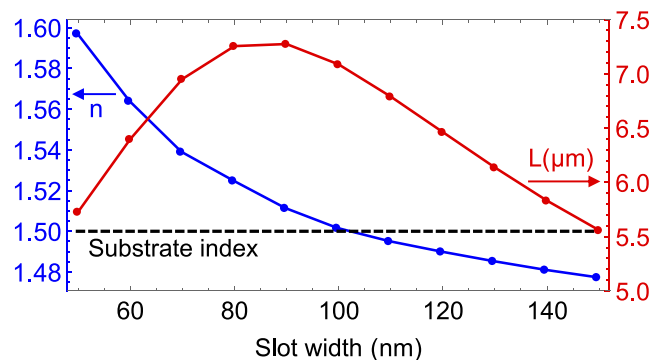


**Fig. 5.** Calculated effective index (blue curve) and propagation length (red curve) of the PSW slot mode as a function of gap size.

#### 4. Conclusion

We have fabricated plasmonic slot waveguides in single-crystalline and poly-crystalline gold films with slot widths down to 50 nm. The effective mode indices and the propagation lengths were experimentally determined by amplitude- and phase resolved near-field measurements with a scattering-type scanning near-field optical microscope. We find that the quality of the gold film has a profound impact for small gap widths for which Ohmic losses are the dominant loss channel. In particular, we observe that the propagation length can be improved by almost a factor of two by choosing a high-quality single-crystalline gold film. In contrast, for gap widths exceeding 100 nm, the waveguides in single-crystalline and poly-crystalline gold films show a comparable performance since leakage radiation into the substrate becomes the dominant loss channel. The latter could be suppressed by embedding the gold film in a symmetric dielectric environment, e.g., by coating the gold film with a spin-on-dielectric [20]. One might argue that the size of the gold flakes could be insufficient for future applications. However, since the typical lateral dimensions of a single-crystalline gold flake are larger than the SPP propagation length, we expect that this aspect only becomes a limitation if one wants to combine many waveguides on a chip. In such a scenario, one could however connect the plasmonic waveguides with low-loss three-dimensional dielectric waveguides, e.g., printed by laser lithography, and use several flakes.

#### Funding

Deutsche Forschungsgemeinschaft (LI 1641/5-1, SFB TR 185 (project A3)).

#### Acknowledgements

The authors acknowledge Mario Hentschel from the University of Stuttgart for support regarding the sample fabrication.

#### Disclosures

The authors declare no conflicts of interest.

#### References

1. D. K. Gramotnev and S. I. Bozhevolnyi, "Plasmonics beyond the diffraction limit," *Nat. Photonics* **4**(2), 83–91 (2010).
2. R. F. Oulton, V. J. Sorger, T. Zentgraf, R.-M. Ma, C. Gladden, L. Dai, G. Bartal, and X. Zhang, "Plasmon lasers at deep subwavelength scale," *Nature* **461**(7264), 629–632 (2009).
3. A. Melikyan, L. Alloatti, A. Muslija, D. Hillerkuss, P. C. Schindler, J. Li, R. Palmer, D. Korn, S. Muehlbrandt, D. Van Thourhout, B. Chen, R. Dinu, M. Sommer, C. Koos, M. Kohl, W. Freude, and J. Leuthold, "High-speed plasmonic phase modulators," *Nat. Photonics* **8**(3), 229–233 (2014).
4. D. K. Gramotnev, K. C. Vernon, and D. F. P. Pile, "Directional coupler using gap plasmon waveguides," *Appl. Phys. B* **93**(1), 99–106 (2008).
5. M. Thomaschewski, Y. Yang, C. Wolff, A. S. Roberts, and S. I. Bozhevolnyi, "On-chip detection of optical spin-orbit interactions in plasmonic nanocircuits," *Nano Lett.* **19**(2), 1166–1171 (2019).
6. Y. C. Jun, R. D. Kekatpure, J. S. White, and M. L. Brongersma, "Nonresonant enhancement of spontaneous emission in metal-dielectric-metal plasmon waveguide structures," *Phys. Rev. B* **78**(15), 153111 (2008).
7. D. E. Chang, A. S. Sørensen, P. Hemmer, and M. Lukin, "Strong coupling of single emitters to surface plasmons," *Phys. Rev. B* **76**(3), 035420 (2007).
8. A. Akimov, A. Mukherjee, C. Yu, D. Chang, A. Zibrov, P. Hemmer, H. Park, and M. Lukin, "Generation of single optical plasmons in metallic nanowires coupled to quantum dots," *Nature* **450**(7168), 402–406 (2007).
9. J. Dorfmueller, R. Vogelgesang, W. Khunsin, C. Rockstuhl, C. Etrich, and K. Kern, "Plasmonic nanowire antennas: experiment, simulation, and theory," *Nano Lett.* **10**(9), 3596–3603 (2010).
10. J.-C. Weeber, A. Dereux, C. Girard, J. R. Krenn, and J.-P. Goudonnet, "Plasmon polaritons of metallic nanowires for controlling submicron propagation of light," *Phys. Rev. B* **60**(12), 9061–9068 (1999).
11. J. R. Krenn, B. Lamprecht, H. Ditlbacher, G. Schider, M. Salerno, A. Leitner, and F. R. Aussenegg, "Non-diffraction-limited light transport by gold nanowires," *Europhys. Lett.* **60**(5), 663–669 (2002).
12. P. Berini, "Plasmon-polariton waves guided by thin lossy metal films of finite width: Bound modes of symmetric structures," *Phys. Rev. B* **61**(15), 10484–10503 (2000).

13. V. A. Zenin, R. Malureanu, I. P. Radko, A. V. Lavrinenko, and S. I. Bozhevolnyi, "Near-field characterization of bound plasmonic modes in metal strip waveguides," *Opt. Express* **24**(5), 4582–4590 (2016).
14. M. L. Brongersma, J. W. Hartman, and H. A. Atwater, "Electromagnetic energy transfer and switching in nanoparticle chain arrays below the diffraction limit," *Phys. Rev. B* **62**(24), R16356 (2000).
15. S. A. Maier, P. G. Kik, H. A. Atwater, S. Meltzer, E. Harel, B. E. Koel, and A. A. Requicha, "Local detection of electromagnetic energy transport below the diffraction limit in metal nanoparticle plasmon waveguides," *Nat. Mater.* **2**(4), 229–232 (2003).
16. D. F. P. Pile, T. Ogawa, D. K. Gramotnev, T. Okamoto, M. Haraguchi, M. Fukui, and S. Matsuo, "Theoretical and experimental investigation of strongly localized plasmons on triangular metal wedges for subwavelength waveguiding," *Appl. Phys. Lett.* **87**(6), 061106 (2005).
17. I. V. Novikov and A. A. Maradudin, "Channel polaritons," *Phys. Rev. B* **66**(3), 035403 (2002).
18. D. F. P. Pile and D. K. Gramotnev, "Channel plasmon-polariton in a triangular groove on a metal surface," *Opt. Lett.* **29**(10), 1069–1071 (2004).
19. G. Veronis and S. Fan, "Guided subwavelength plasmonic mode supported by a slot in a thin metal film," *Opt. Lett.* **30**(24), 3359–3361 (2005).
20. G. Veronis and S. Fan, "Modes of subwavelength plasmonic slot waveguides," *J. Lightwave Technol.* **25**(9), 2511–2521 (2007).
21. C. Rewitz, G. Razinkas, P. Geisler, E. Krauss, S. Goetz, M. Pawłowska, B. Hecht, and T. Brixner, "Coherent control of plasmon propagation in a nanocircuit," *Phys. Rev. Appl.* **1**(1), 014007 (2014).
22. K. C. Y. Huang, M.-K. Seo, T. Sarmiento, Y. Huo, J. S. Harris, and M. L. Brongersma, "Electrically driven subwavelength optical nanocircuits," *Nat. Photonics* **8**(3), 244–249 (2014).
23. C. Schörner, S. Adhikari, and M. Lippitz, "A single-crystalline silver plasmonic circuit for visible quantum emitters," *Nano Lett.* **19**(5), 3238–3243 (2019).
24. M. Blauth, M. Jürgensen, G. Vest, O. Hartwig, M. Precht, J. Cerne, J. J. Finley, and M. Kaniber, "Coupling single photons from discrete quantum emitters in wave2 to lithographically defined plasmonic slot waveguides," *Nano Lett.* **18**(11), 6812–6819 (2018).
25. S. I. Bozhevolnyi, V. S. Volkov, E. Devaux, J.-Y. Laluet, and T. W. Ebbesen, "Channel plasmon subwavelength waveguide components including interferometers and ring resonators," *Nature* **440**(7083), 508–511 (2006).
26. R. Esteban, R. Vogelgesang, J. Dorfmueller, A. Dmitriev, C. Rockstuhl, C. Etrich, and K. Kern, "Direct near-field optical imaging of higher order plasmonic resonances," *Nano Lett.* **8**(10), 3155–3159 (2008).
27. R. L. Olmon, P. M. Krenz, A. C. Jones, G. D. Boreman, and M. B. Raschke, "Near-field imaging of optical antenna modes in the mid-infrared," *Opt. Express* **16**(25), 20295–20305 (2008).
28. M. Schnell, A. Garcia-Etxarri, J. Alkorta, J. Aizpurua, and R. Hillenbrand, "Phase-resolved mapping of the near-field vector and polarization state in nanoscale antenna gaps," *Nano Lett.* **10**(9), 3524–3528 (2010).
29. T. Neuman, P. Alonso-González, A. Garcia-Etxarri, M. Schnell, R. Hillenbrand, and J. Aizpurua, "Mapping the near fields of plasmonic nanoantennas by scattering-type scanning near-field optical microscopy," *Laser Photonics Rev.* **9**(6), 637–649 (2015).
30. M. Spasenović, D. van Oosten, E. Verhagen, and L. Kuipers, "Measurements of modal symmetry in subwavelength plasmonic slot waveguides," *Appl. Phys. Lett.* **95**(20), 203109 (2009).
31. A. Andryieuski, V. A. Zenin, R. Malureanu, V. S. Volkov, S. I. Bozhevolnyi, and A. V. Lavrinenko, "Direct Characterization of Plasmonic Slot Waveguides and Nanocouplers," *Nano Lett.* **14**(7), 3925–3929 (2014).
32. V. A. Zenin, A. Andryieuski, R. Malureanu, I. P. Radko, V. S. Volkov, D. K. Gramotnev, A. V. Lavrinenko, and S. I. Bozhevolnyi, "Boosting local field enhancement by on-chip nanofocusing and impedance-matched plasmonic antennas," *Nano Lett.* **15**(12), 8148–8154 (2015).
33. Y. Chen, V. A. Zenin, K. Leosson, X. Shi, M. G. Nielsen, and S. I. Bozhevolnyi, "Efficient interfacing photonic and long-range dielectric-loaded plasmonic waveguides," *Opt. Express* **23**(7), 9100–9108 (2015).
34. J.-S. Huang, V. Callegari, P. Geisler, C. Brüning, J. Kern, J. C. Prangsma, X. Wu, T. Feichtner, J. Ziegler, P. Weinmann, M. Kamp, A. Forchel, P. Biagioni, U. Sennhauser, and B. Hecht, "Atomically flat single-crystalline gold nanostructures for plasmonic nanocircuitry," *Nat. Commun.* **1**(1), 150 (2010).
35. M. Kuttge, E. Vesseur, J. Verhoeven, H. Lezec, H. Atwater, and A. Polman, "Loss mechanisms of surface plasmon polaritons on gold probed by cathodoluminescence imaging spectroscopy," *Appl. Phys. Lett.* **93**(11), 113110 (2008).
36. Q. Ai, L. Gui, D. Paone, B. Metzger, M. Mayer, K. Weber, A. Fery, and H. Giessen, "Ultrannarrow second-harmonic resonances in hybrid plasmon-fiber cavities," *Nano Lett.* **18**(9), 5576–5582 (2018).
37. M. I. Stockman, K. Kneipp, S. I. Bozhevolnyi, S. Saha, A. Dutta, J. Ndukaife, N. Kinsey, H. Reddy, U. Guler, V. M. Shalaev, A. Boltasseva, B. Gholipour, H. N. S. Krishnamoorthy, K. F. MacDonald, C. Soci, N. I. Zheludev, V. Savinov, R. Singh, P. Groß, C. Lienau, M. Vadai, M. L. Solomon, D. R. Barton, M. Lawrence, J. A. Dionne, S. V. Boriskina, R. Esteban, J. Aizpurua, X. Zhang, S. Yang, D. Wang, W. Wang, T. W. Odom, N. Accanto, P. M. de Roque, I. M. Hancu, L. Piatkowski, N. F. van Hulst, and M. F. Kling, "Roadmap on plasmonics," *J. Opt.* **20**(4), 043001 (2018).
38. J. H. Park, P. Ambwani, M. Manno, N. C. Lindquist, P. Nagpal, S.-H. Oh, C. Leighton, and D. J. Norris, "Single-crystalline silver films for plasmonics," *Adv. Mater.* **24**(29), 3988–3992 (2012).
39. C.-Y. Wang, H.-Y. Chen, L. Sun, W.-L. Chen, Y.-M. Chang, H. Ahn, X. Li, and S. Gwo, "Giant colloidal silver crystals for low-loss linear and nonlinear plasmonics," *Nat. Commun.* **6**(1), 7734 (2015).

40. H. Ditlbacher, A. Hohenau, D. Wagner, U. Kreibig, M. Rogers, F. Hofer, F. R. Aussenegg, and J. R. Krenn, "Silver nanowires as surface plasmon resonators," *Phys. Rev. Lett.* **95**(25), 257403 (2005).
41. P. Kusar, C. Gruber, A. Hohenau, and J. R. Krenn, "Measurement and reduction of damping in plasmonic nanowires," *Nano Lett.* **12**(2), 661–665 (2012).
42. E. Krauss, R. Kullock, X. Wu, P. Geisler, N. Lundt, M. Kamp, and B. Hecht, "Controlled growth of high-aspect-ratio single-crystalline gold platelets," *Cryst. Growth Des.* **18**(3), 1297–1302 (2018).
43. N. Ocelic, A. Huber, and R. Hillenbrand, "Pseudoheterodyne detection for background-free near-field spectroscopy," *Appl. Phys. Lett.* **89**(10), 101124 (2006).
44. P. B. Johnson and R.-W. Christy, "Optical constants of the noble metals," *Phys. Rev. B* **6**(12), 4370–4379 (1972).